

Title: A Theoretical investigation of the recruitment of Sodium channels to the Axon Initial Segment (AIS) in neurons

Don Kulasiri^{*a}

Abstract

The axon initial segment (AIS) in neurons plays a vital role in initiating action potentials, primarily due to the high density of voltage-gated sodium (Nav) channels concentrated in this region. These Nav channels contain multiple serine residues that mediate their recruitment to the AIS through interactions with ankyrin-G (AnkG). AnkG plays a pivotal role in neurodegenerative diseases such as Alzheimer's, and it is important to understand the dynamics of its interactions with other proteins. In this paper, we develop a theoretical approach to understand the roles of two AIS proteins—casein kinase 2 (CK2) and AnkG—in facilitating Nav channel recruitment to the AIS membrane by firstly modelling the CK2 phosphorylation of Nav and then the binding of AnkG to phosphorylated Nav. Given the structure of Nav, we develop a conceptual model for the mathematical models based on well-defined macro- and micro- states of Nav that participate in elementary reactions simultaneously. The results of the models are discussed in graphical manner to unravel the complexity associated with the AIS dynamics and the dependence of associated kinetic coefficients.

Keywords: Axon initial segment (AIS); theoretical model; Sodium channels; Ankyrin-G, micro-states; macro-states; mathematical modelling; phosphorylation; CK2

*Corresponding author: don.kulasiri@lincoln.ac.nz

^a Centre for Advanced Computational Solutions (C-fACS)

Lincoln University

Lincoln, Canterbury

New Zealand

1. Introduction and background

Action potentials (APs) facilitate the transmission of signals between neurons, and they propagate along the axon toward the presynaptic terminals, where they enable signal transfer to postsynaptic neurons. Multiple studies have demonstrated that action potentials originate at the axon initial segment (AIS), a region lacking myelination located at the proximal end of the axon (Lemaillet et al., 2003; Rasband, 2009; Kole and Stuart, 2012; Gullledge and Bravo, 2016) (Figure 1A). The AIS typically extends ~10 to 60 μm from the axon hillock with a diameter of 1.5 μm giving a volume of ~18-106 (μm)³ (Kole et al., 2008; Buffington and Rasband, 2011; Kole and Stuart, 2012; Leterrier et al., 2015; Jones and Svitkina, 2016; Nelson and Jenkins, 2017; Fan and Markram, 2019).

The AIS contains several key proteins, including voltage-gated sodium channels (Nav), voltage-gated potassium channels (Kv), microtubules (MTs), casein kinase 2 (CK2), and ankyrin-G (AnkG) (Figure 1B). Among these, AnkG is particularly critical, as it is required for the localization of other proteins—such as Kv, Nav, Neurofascin 186 (NF186), and Neuronal Cell Adhesion Molecules (NrcAM)—within the AIS (Hedstrom et al., 2008; Jones and Svitkina, 2016). The AIS is also composed of three membrane systems: the plasma membrane, the spectrin-actin membrane, and the microtubule-associated membrane. Each of these contributes to creating conditions that support the initiation of action potentials (APs) at the AIS. AnkG functions as the central organizer of the AIS, with all other AIS proteins either directly or indirectly interacting with it (Zhang and Bennet, 1998; Zhou et al., 1998; Hedstrom et al., 2008; Cunha and Mohler, 2009; Nelson and Jenkins, 2017). The N-terminal region of AnkG, known as the membrane-binding domain, anchors voltage-gated sodium (Nav) channels and Kv7.2/7.3 potassium channels (Nelson and Jenkins, 2017; Buffington and Rasband, 2011). Most proteins that interact with AnkG at the AIS contain a specific amino acid sequence, termed the AIS motif, with the exception of Kv1.1 and Kv1.2 channels (Schafer et al., 2009). Instead of AnkG, the localization of Kv1.1 and Kv1.2 channels at the AIS relies on the postsynaptic density protein 93 (PSD-93) (Leterrier and Dargent, 2014; Yoshimura and Rasband, 2014). Following the membrane-binding domain, AnkG contains a spectrin-binding domain that mediates its interaction with βIV -spectrin (Jones and Svitkina, 2016). Additionally, AnkG constrains microtubule bundles within the AIS through its interaction with the end-binding protein 3 (EB3) (Nakata and Hirokawa, 2003; Jones and Svitkina, 2016). Experimental studies have shown that the high density of Nav channels in the AIS is critical for AP initiation (Kole et al., 2012; Jones and Svitkina, 2016) and that this accumulation is regulated by AnkG in conjunction with phosphorylation events mediated by casein kinase 2 (CK2) (Brechet et al., 2008). Moreover, CK2 has been shown to play an active role in the AIS, particularly in promoting the clustering of Nav channels within this region (Brechet et al., 2008; Nishi et al., 2014; Xu and Cooper, 2015).

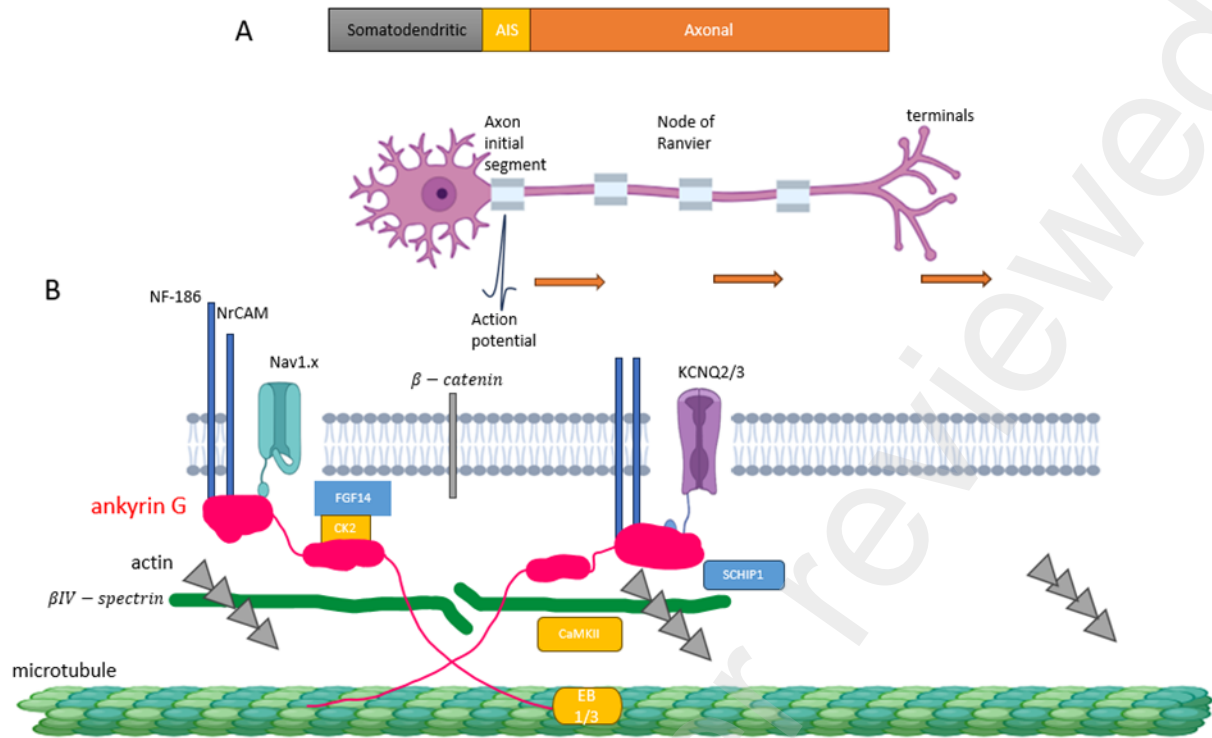


Figure 1. The components of the Axon Initial Segment (AIS) region.

(A) Neurons process incoming signals within the somatodendritic area. The AIS, situated at the start of the axon, generates action potentials that travel to terminals and regenerates at nodes of Ranvier between internodes. (B) The structural organization of the AIS is primarily centred around AnkG, which anchors β IV-spectrin, a protein that associates with actin filaments. AnkG also forms connections with Nav1.x and Kv7.2/7.3 ion channels, as well as with the adhesion molecules NF-186 and NrCAM. Additionally, microtubules are tethered to AnkG via EB1/3 proteins, while SCHIP1 serves as another AnkG-binding partner.

Casein kinase 2 (CK2) is a serine/threonine-specific, acidophilic kinase that phosphorylates various proteins within the AIS (Meggio and Pinna, 2003). Notably, CK2 is constitutively active and does not require second messengers or prior phosphorylation for its activation (Meggio and Pinna, 2003; Bian et al., 2013). During neuronal development, CK2 is present in neurons even before axon formation, and experimental studies have shown that inhibiting CK2 can result in approximately a 30% reduction in axon length (Sa´nchez-Ponce et al., 2012). CK2 plays a pivotal role in facilitating the recruitment of voltage-gated sodium (Nav) channels to the AIS by promoting their phosphorylation, which enhances their binding affinity to AnkG (Rasband, 2008; Yamada and Kuba, 2016).

Alterations in neuronal signalling have been implicated in numerous neurological disorders (Figure 2), including Alzheimer’s disease (AD), epilepsy, schizophrenia, and bipolar disorder (Buffington and Rasband, 2011; Kaphzan et al., 2011; Bi et al., 2012; Harty et al., 2013; Rueckert et al., 2013; Peltola et al., 2016). Several studies have demonstrated a correlation between AD pathology and alterations in proteins localized to the AIS, with observed reductions in AnkG and voltage-gated sodium (Nav) channels in postmortem AD brain tissue (Kim et al., 2007; Sun et al., 2014). Notably, cleavage of Nav

channels has been associated with increased production of amyloid β ($A\beta$) peptides, the principal components of amyloid plaques characteristic of AD (Kim et al., 2007; Kovacs et al., 2010). Furthermore, loss of AnkG within the AIS may contribute to AD pathogenesis by disrupting intracellular trafficking processes, potentially via the effects on molecular motors such as kinesin and dynein (Kim et al., 2007; Sun et al., 2014). Therefore, it is important to understand the mechanistic behaviour of the phosphorylation of Nav channels, and the binding of phosphorylated Nav to AnkG within the AIS.

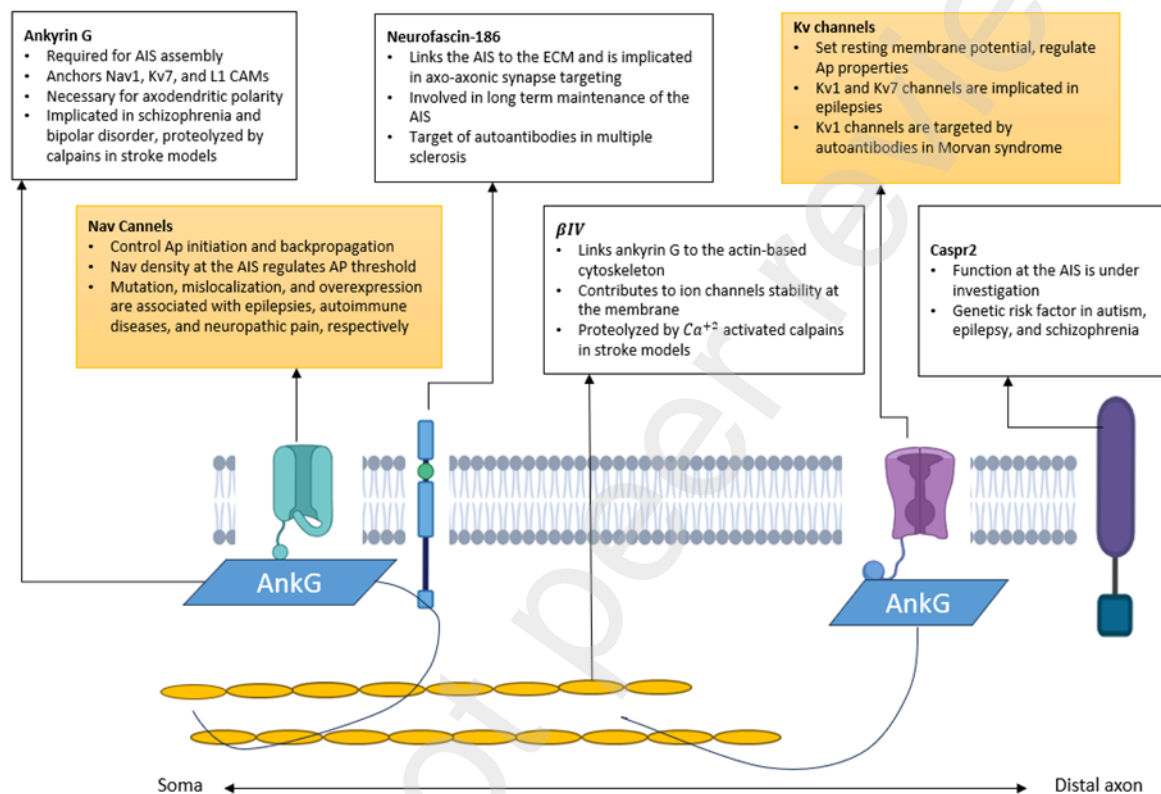


Figure 2. Dysfunctions in AIS are related to many neurological disorders.

Mathematical modelling of phosphorylation

Salazar and Höfer (2009) reviewed mathematical frameworks used to model phosphorylation processes, a reversible post-translational modification mediated by kinases and phosphatases, with an emphasis on the limitations of conventional enzyme kinetics and the importance of mechanistic modelling. Multisite phosphorylation is critical in many intra- and inter- cellular processes such as T-cell receptor activation, nuclear transport of transcription factors (e.g., NFAT), and cell cycle regulation (e.g., Sic1 degradation). However, traditional Michaelis–Menten kinetics often assume enzyme concentrations are negligible compared to substrates, which is rarely true for these processes. Instead, mechanistic models based on mass-action kinetics for elementary reactions are better suited for accurately describing complex phosphorylation dynamics, particularly when multiple sites, enzymes, or feedback mechanisms are involved. Their review also delves into sequential and random site processing and between distributive and processive enzyme mechanisms, within multisite phosphorylation. The authors illustrate how the number and arrangement of phosphorylation sites,

together with enzyme behaviour, shape system responses—such as ultra sensitivity, graded or switch-like transitions, and bi-stability. In essence, they underscore how mechanistic mathematical models can help decode the dynamic complexity of phosphorylation-based regulation in biological systems.

Stepanov et al. (2018) presents the first mechanistic mathematical model of multisite phosphorylation and dephosphorylation of tau protein—a key factor in tauopathies such as Alzheimer’s disease. Using a probability-based approach, the model captures how tau is phosphorylated by GSK3 β and CDK5, with PKA acting as a priming kinase, and dephosphorylated by PP2A. The model accurately reproduces short-term in vitro kinetics by allowing partial phosphorylation and combining random and sequential mechanisms, offering biologically realistic predictions while avoiding the combinatorial complexity typical of traditional models. Key findings include: PKA priming enhances phosphorylation, especially via GSK3 β ; S396 and S404 phosphorylation (PHF1 sites) is highly sensitive to GSK3 β and represents potential therapeutic targets; and the model aids identification of specific kinase targets and site-sensitive biomarkers, with implications for drug development and diagnostic precision in Alzheimer’s disease. This model serves as a foundational tool for systems modelling of tau-related pathologies.

A mathematical model rooted in these dynamics would help us to better understand the neurodegenerative diseases by exploring the combinations of factors that would influence AP generation and help the experimentalists to guide their research. We develop such a theoretical model firstly modelling the CK2-mediated phosphorylation of Nav channels to investigate the behaviours of phosphorylated channels and then we proceed to include the AnkG binding to appropriately phosphorylated channels. The behaviours of our model align qualitatively with existing literature connecting Nav channel alterations to AnkG binding, highlighting a mechanistic and mathematical link to AD pathology (Kim et al., 2007; Kovacs et al., 2010), for example.

2. Development of Conceptual and Mathematical models

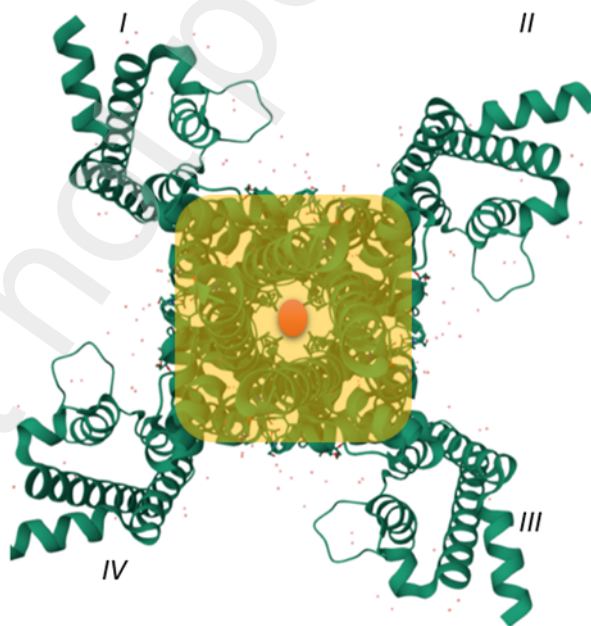
A functional model of Sodium channel

The Na_v channel has four domains (I-IV) and every domain has six transmembrane segments (TS1-TS6) (Jones and Svitkina, 2016) (Figure 3). TS1- TS4 of all the four domains are sensitive towards voltage and are known as voltage sensing segments. However, the TS5-TS6 segments of all domains are known as pore forming segments and are responsible for the entry of Na⁺ ions. The ankyrin-binding motif (ABM) between domains II and III binds to the membrane-binding domain (MBD) of AnkG (Leterrier and Dargent 2014, Xu and Cooper, 2015, Zhou et al., 1998) (Figure 3).

CK2 facilitates the phosphorylation of Na_v channels to increase their affinity towards AnkG before binding (Schafer et al., 2009; Bian et al., 2013; Meggio and Pinna, 2003; Brechet et al., 2008). The

AIS motif is located between the II and III domains of the Na_v channels, and is made up of different 27 amino acids, with four main ones: serine (S) at the positions 1112, 1123, 1124, and 1126; glutamate (E) at the positions 1111 and 1115; and aspartate (D) at the position, 1113. Serine is important because the phosphorylation of Na_v channels is accomplished by CK2, and CK2 is specific for serine or threonine. The presence of negative residues, such as glutamate and aspartate, are also significant because they provide the support for the CK2-mediated phosphorylation of serine. Moreover, glutamate and aspartate assist CK2 in the identification of serine as a target for phosphorylation. Phosphorylation of various sites present in the AIS motif of Na_v channels modulates the channel and its subtypes (Fache et al., 2004). Mutational studies on the four serine sites in Na_v channels showed a significant reduction in Na_v channel concentrations in the AIS. However, a single mutation by replacing each serine with alanine one by one did not alter Na_v channel trafficking(Bréchet et al., 2008, Fache et al., 2004). In contrast, double and triple serine mutations have shown a large reduction in Na_v channel concentrations in the structure of AIS. Out of four serine sites, any single serine mutation, together with a glutamate (E1111) mutation, impairs the segregation of Na_v channels in the AIS structure (Fache et al., 2004). Moreover, the E1111 residue is also shown to be important for Na_v channels trafficking towards AIS. E1111 in the AIS motif is not a phosphorylation site for CK2 but still plays a significant part in Na_v channel trafficking. This may be because of the acidic nature of E1111, which enhances phosphorylation near serine or threonine.

A.



B.

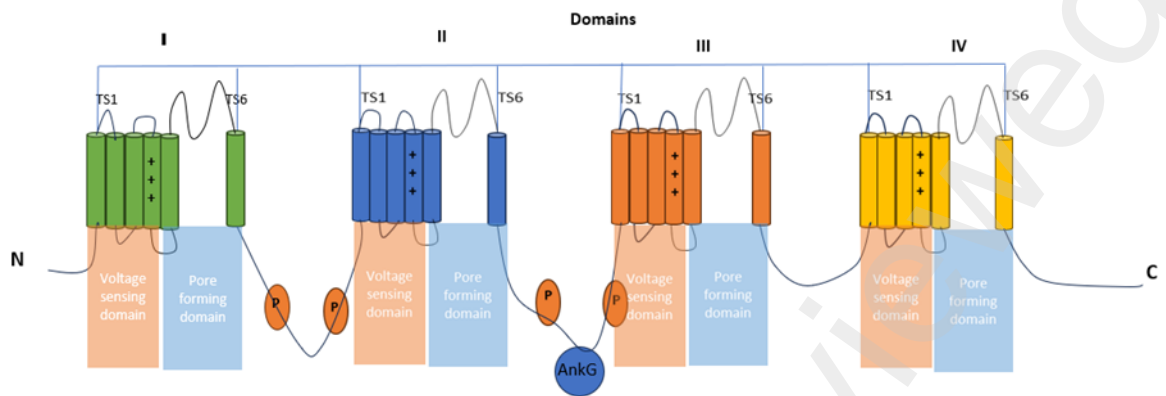


Figure 3. (A) Structure of Nav channel. The green areas on the corners depict the transmembrane segments (TS1-TS4) of the four domains (I-IV), while the yellow portion represents pore-forming segments created by TS5-TS6 in each domain. In the centre, the gap illustrates (orange) the route for Na^+ ions to enter and exit when Nav channels open and close in response to shifts in membrane potential (Catterall, 2014, Cantrell et al., 2018). **(B)** A schematic showing transmembrane segments, four voltage sensing domains, two pore forming domains, and AnkG.

Given the above-mentioned experimental evidence, we conceptualize the microstates of Nav channels based on their CK2 mediated phosphorylation status. To simplify the mathematical modelling, we only consider the influences of four serine phosphorylation sites (1112, 1123, 1124, and 1126), and they are depicted as microstates in the notation $sijkl$ where $i, j, k, l \in (0,1)$. Here $i, j, k,$ and l refer to Serine 1112, 1112, 1124, and 1126 sites respectively, and we assume that influences of E and D relatively negligible compared to those by CK2 phosphorylation sites. Initially at time ($t=0$), we assume that all Nav channels are in unphosphorylated microstates ($s0000$), by depicting phosphorylation of a transmembrane segment as 1 using binary notation, then at any given time there are ($2^4=$)16 microstates of Nav channels. Single site phosphorylation states are $s1000, s0100, s0010, s0001$; double site states are $s1100, s0110, s1001, s0011, s1010,$ and $s0101$; triple site states are $s1110, s1101, s1011,$ and $s0111$; and four site state is $s1111$. The concentrations of these individual microstates play crucial roles in AnkG binding due to differential affinities; hence it is important to model the phosphorylation of Nav channels using the microstates. The in vitro experimental evidence however points to the fact that (1) none of the Nav species is in of the Na_v species in the model is in the no phosphorylation or single-site phosphorylation conditions; (2) In the double-site phosphorylation, two serine sites are phosphorylated, and there is a total of six combinations; the three combinations, $s1100, s1001,$ and $s1010,$ have stronger affinities towards binding with AnkG due to phosphorylation of the first site, and the affinities of other sites with AnkG may be negligible (Fache et al., 2004; Brechet et al., 2008); (3) In the triple-site phosphorylation conditions, all combinations favour the interaction of Na_v -AnkG, but $s1110, s1101,$ and $s1011$ have distinctly larger affinities than $s0111$ for the same reason; and (4) $s0111$ has a lower affinity because phosphorylation of the remaining three serine sites can cooperatively activate Na_v -AnkG interactions but with a lower binding affinity (Brechet et al., 2008). The fourth Na_v species $s1111$ has the highest affinity towards AnkG according to in-vitro experiments.

Even though we do not have reliable kinetic coefficients, their relativities should reflect these experimental facts reported.

2.1 Development of a mathematical model of phosphorylation of Nav by CK2

As discussed previously, there are 16 microstates of Nav channels at any given time, and CK2 is abundantly associated with the AIS, leading to dynamic interactions between microstates, both phosphorylated and unphosphorylated, and CK2, and phosphorylated microstates in turn bind to AnkG. We assume that all these reactions are reversible and elementary, but the experimental evidence shows that forward affinities are stronger than reverse affinities. This allows us to use mass action kinetics (Salazar and Höfer 2009). We model the phosphorylation first without AnkG binding to develop the theoretical model. We also assume that CK2 phosphorylates a binding site independently to other. Since the reactions occur randomly, we define a probabilistic formulation based on the idea of macro-states consisting of orderly micro-states as given below (Stepanov et al. 2018;):

$$S_{a_1}^j = \sum_{a_2=0}^1 \sum_{a_3=0}^1 \sum_{a_4=0}^1 s a_1 a_2 a_3 a_4, \quad j = 0 \text{ or } 1 \quad (1)$$

where $S_{a_1}^j$ and $s a_1 a_2 a_3 a_4$ refer to the numbers of macro-states and micro-states, respectively.

Eq.(1) means that we have two macro states for the phosphorylation of a_1 site as follows:

$$S_{a_1}^j = \sum_{a_2=0}^1 \sum_{a_3=0}^1 (s a_1 a_2 a_3 0 + s a_1 a_2 a_3 1) = \sum_{a_2=0}^1 (s a_1 a_2 0 0 + s a_1 a_2 0 1 + s a_1 a_2 1 0 + s a_1 a_2 1 1) = s a_1 0 0 0 + s a_1 1 0 0 + s a_1 1 0 1 + s a_1 1 1 0 + s a_1 1 1 1 \quad (2)$$

Hence,

$$S_{a_1}^0 = s 0 0 0 0 + s 0 0 0 1 + s 0 0 1 0 + s 0 0 1 1 + s 0 1 0 0 + s 0 1 0 1 + s 0 1 1 0 + s 0 1 1 1 \quad (3)$$

$$S_{a_1}^1 = s 1 0 0 0 + s 1 0 0 1 + s 1 0 1 0 + s 1 0 1 1 + s 1 1 0 0 + s 1 1 0 1 + s 1 1 1 0 + s 1 1 1 1 \quad (4)$$

We see that $S_{a_1}^0 + S_{a_1}^1$ contains all the microstates, and we denote it by S_{Total} . The macro-variable $S_{a_1}^0$ is phosphorylated into $S_{a_1}^1$ by phosphorylating a_1 site by CK2 in each of the micro-states independent to other sites. This key assumption, which may be realistic in many situations, is the basis of this derivation. Similarly, we write the equations for other six macro-states and their relationships to micro-states as follows:

$$S_{a_2}^0 = s 0 0 0 0 + s 1 0 0 0 + s 0 0 1 0 + s 1 0 1 0 + s 0 0 0 1 + s 1 0 0 1 + s 0 0 1 1 + s 1 0 1 1 \quad (5)$$

$$S_{a_2}^1 = s 0 1 0 0 + s 1 1 0 0 + s 0 1 1 0 + s 1 1 1 0 + s 0 1 0 1 + s 1 1 0 1 + s 0 1 1 1 + s 1 1 1 1 \quad (6)$$

$$S_{a_3}^0 = s 0 0 0 0 + s 1 0 0 0 + s 0 1 0 0 + s 1 1 0 0 + s 0 0 0 1 + s 1 0 0 1 + s 0 1 0 1 + s 1 1 0 1 \quad (7)$$

$$S_{a_3}^1 = s 0 0 1 0 + s 1 0 1 0 + s 0 1 1 0 + s 1 1 1 0 + s 0 0 1 1 + s 1 0 1 1 + s 0 1 1 1 + s 1 1 1 1 \quad (8)$$

$$S_{a_4}^0 = s0000 + s1000 + s0100 + s1100 + s0010 + s1010 + s0110 + s1110 \quad (9)$$

$$S_{a_4}^1 = s0001 + s1001 + s0101 + s1101 + s0011 + s1011 + s0111 + s1111 \quad (10)$$

It is seen that $S_{Total} = S_{a_i}^0 + S_{a_i}^1$ for $i=1,2,3,4$. Because of the independence of phosphorylation of micro-variables, the macro-variable $S_{a_i}^1$ can be considered as the phosphorylated $S_{a_i}^0$ by CK2 but the reactions should be written for individual micro-variable conversions. To reduce the combinatorial complexity that stems from letting the reactions to occur randomly, we use a probabilistic approach to calculate the concentrations of individual micro-states (Borisov et al. 2005). We use the same notation for the species the concentrations in this paper. We see that from Eqs. (3), (5), (8), and (10), $S_{a_1}^0$, $S_{a_2}^0$, $S_{a_3}^1$, and $S_{a_4}^1$ contain s0011, and the phosphorylation of these macro-variables are independent to each other, therefore, the probability of s0011 presence, for example, can be expressed as follows:

$$\frac{s0011}{S_{Total}} = \left(\frac{S_{a_1}^0}{S_{Total}} \right) \left(\frac{S_{a_2}^0}{S_{Total}} \right) \left(\frac{S_{a_3}^1}{S_{Total}} \right) \left(\frac{S_{a_4}^1}{S_{Total}} \right) \quad (11)$$

Then we compute s0011:

$$s0011 = \frac{(S_{a_1}^0)(S_{a_2}^0)(S_{a_3}^1)(S_{a_4}^1)}{(S_{Total})^3} \quad (12)$$

If we first compute Eq. (12), after computing the relevant $S_{a_i}^j$ s, then we avoid having to solve a large number of ordinary differential equations (ODEs) for kinetic reactions. We avoid writing mathematical expressions for the equations to highlight the fact that, for example, s0011 means a sodium channel with last two sites phosphorylated. Affinity of s0011 to CK2 may very well be different to, for example, that of s0000. We can follow Table 1 to compute the concentrations of micro-states.

	$S_{a_1}^0$	$S_{a_1}^1$	$S_{a_2}^0$	$S_{a_2}^1$	$S_{a_3}^0$	$S_{a_3}^1$	$S_{a_4}^0$	$S_{a_4}^1$
S0000	X		X		X		X	
S0100	X			X	X		X	
S0010	X		X			X	X	
S0110	X			X		X	X	
S0001	X		X		X			X
S0101	X			X	X			X
S0011	X		X			X		X
S0111	X			X		X		X
S1000		X	X		X		X	
S1100		X		X	X		X	
S1010		X	X			X	X	
S1110		X		X		X	X	
S1001		X	X		X			X
S1101		X		X	X			X
S1011		X	X			X		X
S1111		X		X		X		X

Table 1. Calculation of micro-state concentration by multiplying the macro-states denoted by ‘X’ along a row and dividing the result by $(S_{Total})^3$. For example, $s1110 = (S_{a_1}^1 S_{a_2}^1 S_{a_3}^1 S_{a_4}^0) / (S_{Total})^3$.

Modelling micro-state phosphorylation by CK2

Let us take the macro-state transformation, $S_{a_1}^0 \rightleftharpoons S_{a_1}^1$ that indicates the phosphorylation of a_1 sites by CK2 in eight micro-states in Eq. (3) into micro-states in Eq. (4). Denoting CK2 by C for notational convenience, we write a kinetic reaction, $S_{a_1}^0 + 8 C \rightleftharpoons S_{a_1}^1$, but this means that the following reaction for micro-state s0000 can be written, as an example: $s0000 + C \rightleftharpoons s1000$. We can write forward and reverse reaction velocities in general as v_{fj}^{ai} and the reverse reaction velocity as v_{rj}^{ai} , $i \in (1, 2, 3, 4)$ and $j \in (1, 2, \dots, 8)$. With this notation, for $s0000 + C \rightleftharpoons s1000$ reaction, we write the following ODEs assuming phosphorylation of individual sites are elementary reactions obeying mass action kinetic law:

$$\frac{ds0000}{dt} = -v_{f1}^{a1} + v_{r1}^{a1} \quad (13)$$

$$\frac{ds1000}{dt} = v_{f1}^{a1} - v_{r1}^{a1} \quad (14)$$

$$\frac{dC}{dt} = -v_{f1}^{a1} + v_{r1}^{a1} \quad (15)$$

where, $v_{f1}^{a1} = k_f^{a1} C s0000$, $v_{r1}^{a1} = k_r^{a1} s1000$ and t is time. k_f^{a1} and k_r^{a1} are kinetic rate constants for forward and reverse reactions. Note that we assume that kinetic rates are the same for a specific site in each of 8 micro-states constituting a macro state. Similarly, for the reaction, $s0100 + C \rightleftharpoons s1100$, the following ODEs can be written,

$$\frac{ds0100}{dt} = -v_{f2}^{a1} + v_{r2}^{a1} \quad (16)$$

$$\frac{ds1100}{dt} = v_{f2}^{a1} - v_{r2}^{a1} \quad (17)$$

$$\frac{dC}{dt} = -v_{f2}^{a1} + v_{r2}^{a1} \quad (18)$$

where $v_{f2}^{a1} = k_f^{a1} C s0100$ and $v_{r2}^{a1} = k_r^{a1} s1100$.

CK2 phosphorylates the first site of the 8th micro-state of Eq. (3), $s0111$ into $s1111$, the 8th micro-state of Eq. (4). We can write then,

$$\frac{ds0111}{dt} = -v_{f8}^{a1} + v_{r8}^{a1} \quad (19)$$

$$\frac{ds1111}{dt} = v_{f8}^{a1} - v_{r8}^{a1} \quad (20)$$

$$\frac{dC}{dt} = -v_{f8}^{a1} + v_{r8}^{a1} \quad (21)$$

where $v_{f8}^{a1} = k_f^{a1} C s0111$ and $v_{r8}^{a1} = k_r^{a1} s1111$.

Similar transitions happen simultaneously between other three sets of macro-states: $S_{a_2}^0 \rightleftharpoons S_{a_2}^1$ (Eqs. (5) and (6)); $S_{a_3}^0 \rightleftharpoons S_{a_3}^1$ (Eqs. (7) and (8)); and $S_{a_4}^0 \rightleftharpoons S_{a_4}^1$ (Eqs. (9) and (10)). Note that this formulation does not allow cross transitions across macro-states but all the micro-states transitions, which are assumed to happen randomly and dynamically, are captured within this framework. All the phosphorylation reactions are depicted in the 3-D diagram given in Figure 4.

As we assume 8 micro-states associated with a specific macro-state are independently phosphorylated, we can differentiate Eq. (3),

$$\frac{dS_{a_1}^0}{dt} = \frac{ds0000}{dt} + \frac{ds0100}{dt} + \dots + \frac{ds0111}{dt} \quad (22)$$

$$\frac{dS_{a_1}^0}{dt} = (-v_{f1}^{a1} + v_{r1}^{a1}) + (-v_{f2}^{a1} + v_{r2}^{a1}) + \dots + (-v_{f8}^{a1} + v_{r8}^{a1}) \quad (23)$$

Eq. (23) can be written as,

$$\frac{dS_{a_1}^0}{dt} = - (v_{f_1}^{a_1} + v_{f_2}^{a_1} + \dots + v_{f_8}^{a_1}) + (v_{r_1}^{a_1} + v_{r_2}^{a_1} + \dots + v_{r_8}^{a_1}) \quad (24)$$

Similarly, we can write,

$$\frac{dS_{a_1}^1}{dt} = (v_{f_1}^{a_1} + v_{f_2}^{a_1} + \dots + v_{f_8}^{a_1}) - (v_{r_1}^{a_1} + v_{r_2}^{a_1} + \dots + v_{r_8}^{a_1}) \quad (25)$$

We can write the derivatives of macro-states as follows in terms of reaction velocities:

$$\begin{aligned} \frac{dS_{a_j}^i}{dt} &= - (-1)^i (v_{f_1}^{a_j} + v_{f_2}^{a_j} + \dots + v_{f_8}^{a_j}) + (-1)^i (v_{r_1}^{a_j} + v_{r_2}^{a_j} + \dots + v_{r_8}^{a_j}), \\ a_j &\in (a_1, a_2, a_3, a_4); i \in (0, 1) \end{aligned} \quad (26)$$

For CK2 dynamics associated with each micro-state, we write,

$$\begin{aligned} \frac{dC}{dt} &= - v_{f_1}^{a_1} + v_{r_1}^{a_1} \\ \frac{dC}{dt} &= - v_{f_2}^{a_1} + v_{r_2}^{a_1} \\ &\cdot \\ \frac{dC}{dt} &= - v_{f_8}^{a_1} + v_{r_8}^{a_1} \\ &\cdot \\ &\cdot \\ \frac{dC}{dt} &= - v_{f_8}^{a_4} + v_{r_8}^{a_4} \\ \frac{dC}{dt} &= - v_{f_8}^{a_4} + v_{r_8}^{a_4} \\ &\cdot \\ &\cdot \\ \frac{dC}{dt} &= - v_{f_8}^{a_4} + v_{r_8}^{a_4} \end{aligned}$$

There are 8 equations in each block of macro-state transitions, and we have four such blocks, hence 32 equations all together. We can add these 32 equations together to obtain the following equation:

$$\frac{dC}{dt} = - \left(\frac{1}{32} \right) [(\sum_{a_j=a_1}^{a_4} (v_{f_1}^{a_j} + v_{f_2}^{a_j} + \dots + v_{f_8}^{a_j})) - \sum_{a_j=a_1}^{a_4} (v_{r_1}^{a_j} + v_{r_2}^{a_j} + \dots + v_{r_8}^{a_j})] \quad (27)$$

We can now compute temporal behaviours of macro- and micro- variables by providing appropriate values for kinetic parameters and initial conditions. We have developed a Mathematica[®] (version 14.2) programme to solve the equations. We use finite difference schemes to solve ODEs simultaneously with time intervals of order $<10^{-4}$. The algorithm first computes the macro-states and then uses them to

calculate micro-states, and the algorithm has been implemented for reasonable computational efficiency. The algorithm checks for the mass conservation for Nav and CK2 as the model system is a closed system (See Figure 6). For simplicity of notation, we write $k_f^{ai}=k_{fai}$ and $k_r^{ai}=k_{rai}$, $ai \in (a1,a2,a3,a4)$ hereafter.

2.2 Computational experiments

Our primary interest is in the behaviours of micro-variables with different levels of phosphorylation (single-, two-, three-, and four- phosphorylation) and we assume that all sites are unphosphorylated initially, i.e., all Nav are in s0000, and then CK2 is introduced. These processes happen in the vicinity of AIS outer membrane, and the binding of AnkG to the phosphorylated Nav channels would anchor them to the membrane. (Membrane dynamics are far more complex than the processes we model in this paper, but this is a parsimonious model to understand the binding of Nav to AIS region based on the experimental evidence.) To understand the dynamics of phosphorylation, our computations are based on representative values, not the actual values, of initial conditions, coefficients with appropriate units. The limited number of experiments with different types of neurons reported in literature give a diverse range of coefficients due to different in-vitro conditions and we experiment with these values in the last section of this paper.

A computational experiment: Initial value of CK2 > initial value of Nav (s0000): at t=0, C(0)=2.0; s0000=1.0; $k_f^{a1} \equiv k_{fa1}=0.5$; $k_r^{a1} \equiv k_{ra1}=0.2$; $k_{fa2}=0.5$; $k_{ra2}=0.2$; $k_{fa3}=0.5$; $k_{ra3}=0.2$; $k_{fa4}=0.5$; $k_{ra4}=0.2$; Time interval= $\Delta t=0.0001$; Total time= 7 time units. Note that the coefficients for binding 2.5 times higher than those for unbinding. The results are shown below graphically.

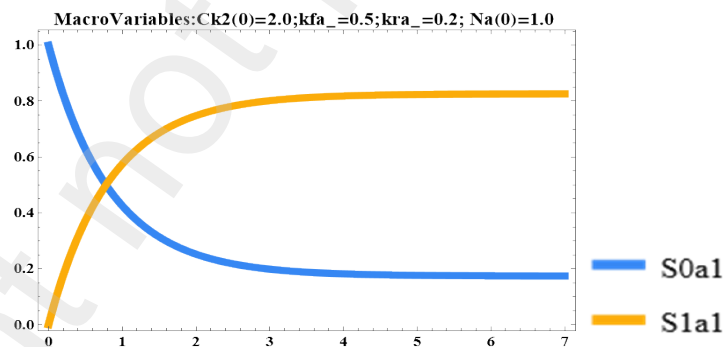


Figure 4. Time courses of Macro-states S_{a1}^0 (=S0a1 for notational convenience) and S_{a1}^1 (=S1a1) for Experiment 01. Note $S_{a1}^0(0) = s0000 = 1.0$ and $S_{a1}^1(0) = 0.0$. S1a1 shows a logistic growth reaching a plateau at 0.8 and S0a1 flattening at 0.2 making the addition of both =1.0, at any given time.

Same graph as in Figure 4 can be obtained (graphs are not shown) for all the other three sets of macro-variables as any set of macro-states contain all the micro-states showing that Nav channels are conserved in the system. We compute the time trajectories of single site phosphorylated micro-states (s1000, s0100, s0010 and s0001) and they are the same because kinetic coefficients for binding and unbinding of CK2 do not change across different sites (see Figure 5A). If they do, we see the differences in the curves. Similarly, Figure 5B shows the trajectories for the double-, triple-, and quadruple- sites

phosphorylated micro-states along with the curve in Figure 5A for the same initial and kinetic coefficients.

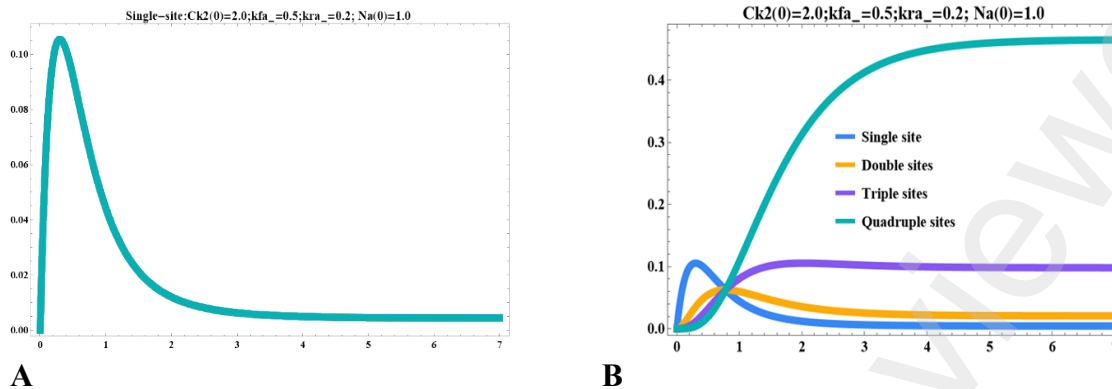


Figure 5. (A) Trajectories for single site phosphorylated micro-states s_{1000} , s_{0100} , s_{0010} , and s_{0001} overlap with each other. (B) Time courses of different levels of phosphorylation of Nav. Single and double sites phosphorylation peak early and the other two plateau at higher levels.

Single site phosphorylated micro-states peak first as expected, double site phosphorylated micro-states peak slightly later within 1 time unit, and triple site phosphorylated micro-states plateaus around its peak level stabilising their level with significance presence in the system (Figure 5B). All the four sites phosphorylated micro-states eventually dominate showing a logistic type of behaviour plateauing at a level almost 4.6 times higher level than that for triple site micro-states. Note that all trajectories cross a single point in the graph at approximately (0.8, 0.06) where all micro-states have equal concentrations due to the same coefficients used in the calculations. Further, we see the rapid decay of s_{0000} (initial level of unphosphorylated Nav), slower decay in CK2, and conservation of total sum of micro-states, i.e., Nav channels within the system (Figure 6).

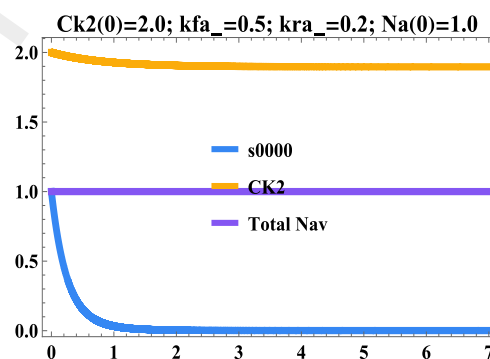


Figure 6. Trajectories of s_{0000} , CK2 and total sum of Nav.

The phosphorylation dynamics change when we use different kinetics coefficients for different sites keeping $k_{fai} > k_{rai}$ ($i=1,2,3,4$). For the same initial condition as before, letting, for example, $k_{fa1}=0.6$, $k_{ra1}=0.3$; $k_{fa2}=0.7$, $k_{ra2}=0.2$; $k_{fa3}=0.4$, $k_{ra3}=0.1$; and $k_{fa4}=0.5$, $k_{ra4}=0.1$, we obtain the trajectories of single site, double site, triple site, and quadruple site phosphorylated micro-states given in Figures

7, 8, 9, and 10, respectively. It is seen that s0100 peaks higher in Figure 7 because kfa2 is the highest among all followed by s1000 (kfa1=0.6), s0001 (kfa4=0.5), and s0010 (kfa3=0.0.4), respectively. Relatively higher value of kra1 also contributes to lower peak of s1000.

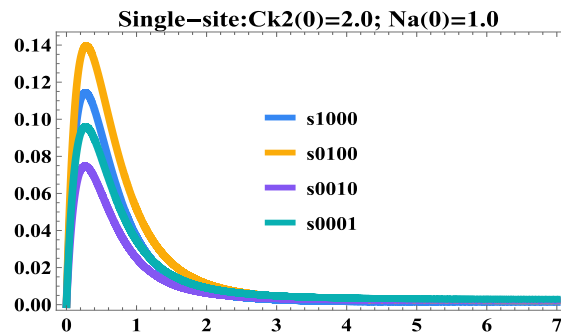


Figure 7. Single site phosphorylated micro-states for kfa1=0.6, kra1=0.3; kfa2=0.7, kra2=0.2; kfa3=0.4, kra3=0.1; and kfa4=0.5, kra4=0.1.

Double site phosphorylated micro-states show more diverse behaviours as combinatorics effects are increased in terms of how the kinetic coefficients influence the system dynamics (Figure 8) but peaks are lower than those in Figure 7.

The kinetic combinatorics influences three site phosphorylated sites similarly (Figure 9) with logistic type plateaus shown for s0111 and s1011; and s1111 shows a robust logistic curve (Figure 10) with a plateau of 0.54.

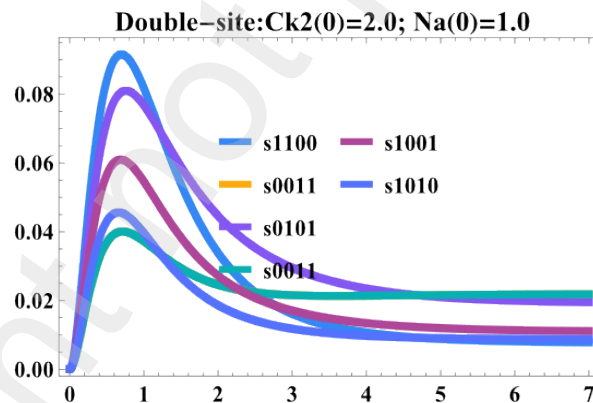


Figure 8. Double site phosphorylated micro-states behaviours for kfa1=0.6, kra1=0.3; kfa2=0.7, kra2=0.2; kfa3=0.4, kra3=0.1; and kfa4=0.5, kra4=0.1.

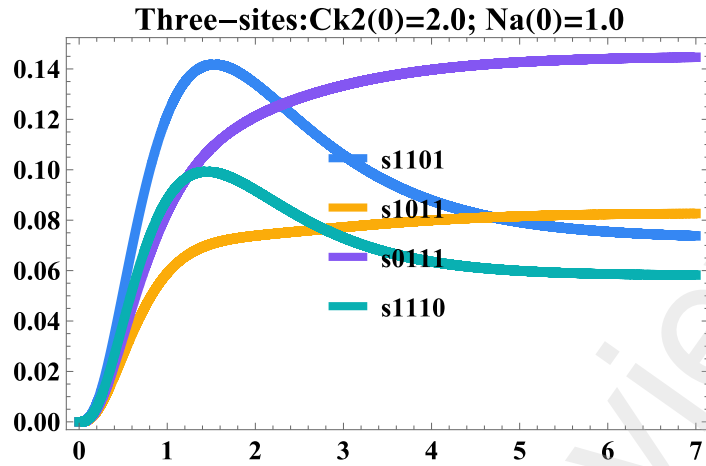


Figure 9. Triple site phosphorylated micro-states behaviours for $k_{fa1}=0.6$, $k_{ra1}=0.3$; $k_{fa2}=0.7$, $k_{ra2}=0.2$; $k_{fa3}=0.4$, $k_{ra3}=0.1$; and $k_{fa4}=0.5$, $k_{ra4}=0.1$.

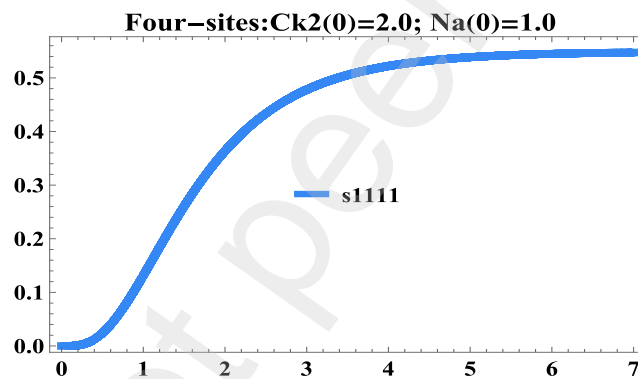


Figure 10. Trajectory of s_{1111} .

Even with $CK2(0)=Nav(0)$ and $CK2(0)<Nav(0)$ macro- and micro- state graphs are similar in shapes with lower peaks and taking more time to reach plateaus (figures not shown). Therefore, the model is robust within diverse ranges of initial conditions and kinetic coefficients. Time trajectories of micro-states reach stable points with the highest plateaus always with s_{1111} and $\{s_{1110}, s_{0111}, s_{1011}, s_{1101}\}$ but other states also have relatively significant values for most of the coefficients tested. In all situations, except for very low initial $CK2$ values compared to $Nav(0)$, s_{0000} reaches zero as time increases. When $CK2(0)=0.1$, $Nav(0)=1.0$, the trajectories of micro-states for $k_{fa1}=k_{fa2}=k_{fa3}=k_{fa4}=0.5$ and $k_{ra1}=k_{ra2}=k_{ra3}=k_{ra4}=0.2$ are given in Figure 11. In this situation, it takes a long time for all sites to be phosphorylated, and single- and double- sites phosphorylated states have relatively higher concentrations.

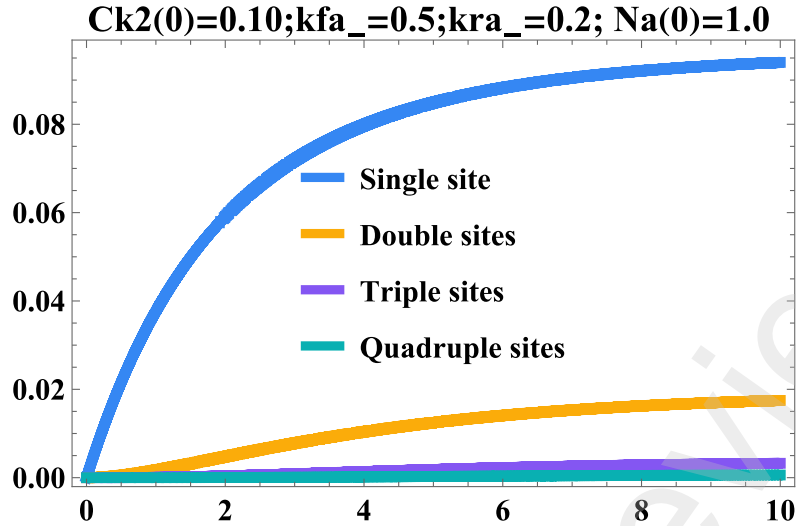


Figure 11. Micro-state trajectories for $CK(0) \ll Na(0)$.

The computational experiments so far discussed show that forward- and reverse- binding affinities play a significant role and to a lesser extent CK2 level influences the phosphorylated Nav channels making them available for AnkG binding and anchoring in the AIS membrane. Therefore, the phosphorylation by CK2 is crucial for the inflow cations into the AIS causing the spiking part of AP in a neuron. These insights from the model corroborate with the experimental data discussed in the last section. In a living organism, fluctuations in kinetics and concentration levels of species are the norm, so micro-states are also in fluctuating states, so APs are affected by the randomness associated with phosphorylation as well as AnkG binding. But it is beyond the scope of this paper to address the effects of fluctuations.

3. Modelling of AnkG binding to the phosphorylated Nav channels

The binding of AnkG to the micro-states of Nav occur simultaneously with the phosphorylation, i.e., it is not a sequential process to the phosphorylation process. This complicates the dynamics, and we assume that AnkG binds to each phosphorylated micro-state as an elementary reaction with mass action kinetics but with distinct forward and reverse binding kinetic coefficients. The experiments showed that affinities of AnkG for micro-states differ depending on the configurations of phosphorylation sites. We assume that when a micro-state is phosphorylated, it is available for AnkG binding without any time delay. Let us consider, the micro-states associated with the two macro-states,

$$S_{a_1}^0 (= s0000 + s0001 + s0010 + s0011 + s0100 + s0101 + s0110 + s0111) \text{ (Eq. (3)), and } S_{a_1}^1$$

$$(= s1000 + s1001 + s1010 + s1011 + s1100 + s1101 + s1110 + s1111) \text{ (Eq. (4)).}$$

The phosphorylation of $s0000$ to $s1000$ is associated with not only CK2 binding but also AnkG binding simultaneously to $s0000$ and $s1000$:

$s0000 + C \rightleftharpoons s1000$ with k_f^{a1} and k_r^{a1} as forward and reverse reaction rates as before, respectively; $s0000 + A \rightleftharpoons s0000A$ where A stands for AnkG and $s0000A$ is AnkG bound $s0000$ with $kf0000$ and $kr0000$ as forward and reverse rate coefficients; and similarly, $s1000 + A \rightleftharpoons s1000A$ where $s1000A$ is AnkG bound $s1000$ with $kf1000$ and $kr1000$ as forward and reverse reaction rate coefficients, respectively. For these reactions, we write the following ODEs:

$$\frac{ds0000}{dt} = -k_f^{a1} C s0000 + k_r^{a1} s1000 \quad (28)$$

$$\frac{ds1000}{dt} = k_f^{a1} C s0000 - k_r^{a1} s1000 \quad (29)$$

$$\frac{ds0000}{dt} = -(kf0000) A s0000 + (kr0000) s0000A \quad (30)$$

$$\frac{ds1000}{dt} = -(kf1000) A s1000 + (kr1000) s1000A \quad (31)$$

$$\frac{dA}{dt} = -(kf0000) A s0000 + (kr0000) s0000A \quad (32)$$

$$\frac{dA}{dt} = -(kf1000) A s1000 + (kr1000) s1000A \quad (33)$$

$$\frac{dC}{dt} = -k_f^{a1} C s0000 + k_r^{a1} s1000 \quad (34)$$

$$\frac{ds0000A}{dt} = (kf0000) A s0000 - (kr0000) s0000A \quad (35)$$

$$\frac{ds1000A}{dt} = (kf1000) A s1000 - (kr1000) s1000A \quad (36)$$

Considering macro states $S_{a_1}^0$ and $S_{a_1}^1$, and we have 8 sets of ODEs for all the micro-states, and there are altogether 4 macro-states, with total of 32 ODEs for elementary reactions.

We get the following equations for the derivatives of $s0000$ and $s1000$ after some algebraic manipulations of Eqs. (28)- (36).

$$\frac{ds0000}{dt} = \left(\frac{1}{2}\right) \left[(-k_f^{a1} C s0000 + k_r^{a1} s1000) + \frac{dA}{dt} \right] \quad (37)$$

$$\frac{ds1000}{dt} = \left(\frac{1}{2}\right) \left[(k_f^{a1} C s0000 - k_r^{a1} s1000) + \frac{dA}{dt} \right] \quad (38)$$

Now considering all the eight macro-states, we derive the following ODE for the derivatives of macro states, $S_{a_1}^0$ and $S_{a_1}^1$:

$$\frac{dS_{a1}^0}{dt} = \left(\frac{1}{2}\right) \left[-k_f^{a1} C S_{a1}^0 + k_r^{a1} S_{a1}^1 + 8 \frac{dA}{dt} \right] \quad (39)$$

$$\frac{dS_{a1}^1}{dt} = \left(\frac{1}{2}\right) \left[k_f^{a1} C S_{a1}^0 - k_r^{a1} S_{a1}^1 + 8 \frac{dA}{dt} \right] \quad (40)$$

For 8 macro-states we write in general,

$$\frac{dS_{ai}^j}{dt} = \left(\frac{1}{2}\right) \left[(-1)^j (-k_f^{ai} C S_{ai}^0 + k_r^{ai} S_{ai}^1) + 8 \frac{dA}{dt} \right], j \in (0,1), ai \in (a1,a2,a3,a4) \quad (41)$$

We solve for A from Eq. (40) which is derived by summing equations for the derivatives of A across all the four macro-states.

$$\frac{dA}{dt} = \left(\frac{1}{64}\right) \left[- (kf0000 s0000 + \dots + kf0111 s0111)A \dots - (kf0000 s0000 + \dots + kf1110 s1110)A - \dots + (kr0000 s0000 + \dots + kr0111 s0111)A \dots \right] \quad (42)$$

$$\frac{dA}{dt} = \left(\frac{1}{64}\right) \sum_{a1,a2,a3,a4} \left[- (kfa1a2a3a4 (sa1a2a3a4))A + (kra1a2a3a4 (sa1a2a3a4A)) \right], a1,a2,a3,a4 \in (0,1) \quad (43)$$

In Eq. (43), the summation is taken over the combinations of $(a1, a2, a3, a4)$ related to each macro-state.

We can derive the following ODE for CK2 using the macro-states:

$$\frac{dC}{dt} = \left(\frac{1}{32}\right) \left[- (k_f^{a1} S_{a1}^0 + k_f^{a2} S_{a2}^0 + k_f^{a3} S_{a3}^0 + k_f^{a4} S_{a4}^0) C + (k_r^{a1} S_{a1}^1 + k_r^{a2} S_{a2}^1 + k_r^{a3} S_{a3}^1 + k_r^{a4} S_{a4}^1) \right] \quad (44)$$

Using the above equations and Table 1, we numerically solve for the time trajectories for micro-states, macro-states, phosphorylated micro-states, AnkG, CK2, and AnkG bound micro-states, which are membrane-bound and directly associated with AP.

We develop a Mathematica[®] program to solve the ODEs using a finite difference scheme with time interval of <0.0001-time units as before, and the scheme is stable for the ranges of parameters in the model, i.e., initial conditions and kinetic coefficients.

3.1 Computational experiments

Computational experiments show similar behaviours of phosphorylated micro-states and AnkG bound phosphorylated micro-states are of more interest to us as they are bound to the AIS. For example,

Figures 12 and 13 show AnkG bound micro-states for a set of coefficients: $s_{0000}(0)=5.00$; $CK2_{zero}=2.0$; $k_{fa1}=0.5$; $k_{ra1}=0.2$; $k_{fa2}=0.5$; $k_{ra2}=0.2$; $k_{fa3}=0.5$; $k_{ra3}=0.2$; $k_{fa4}=0.5$; $k_{ra4}=0.2$; $\Delta T=0.0001$; $AnkG_{zero}=1.0$; $k_{f0000}=0.0001$; $k_{f0100}=0.001$; $k_{f0010}=0.001$; $k_{f0110}=0.002$; $k_{f0001}=0.002$; $k_{f0101}=k_{f0011}=0.002$; $k_{f0111}=0.003$; $k_{f1000}=0.001$; $k_{f1100}=k_{f1010}=0.002$; $k_{f1110}=0.003$; $k_{f1001}=0.002$; $k_{f1101}=k_{f1011}=0.003$; $k_{f1111}=0.004$; $k_{r0000}=0.0001$; and $k_{r0100}=k_{r0010}=k_{r0110}=k_{r0001}=k_{r0101}=k_{r0011}=k_{r0111}=k_{r1000}=k_{r1100}=k_{r1010}=k_{r1110}=k_{r1001}=k_{r1101}=k_{r1011}=k_{r1111}=0.0001$. Here we use a higher initial sodium channel levels and AnkG binding and unbinding coefficients are orders of magnitude less than those for CK2 binding and unbinding based on previous discussion on experimental findings.

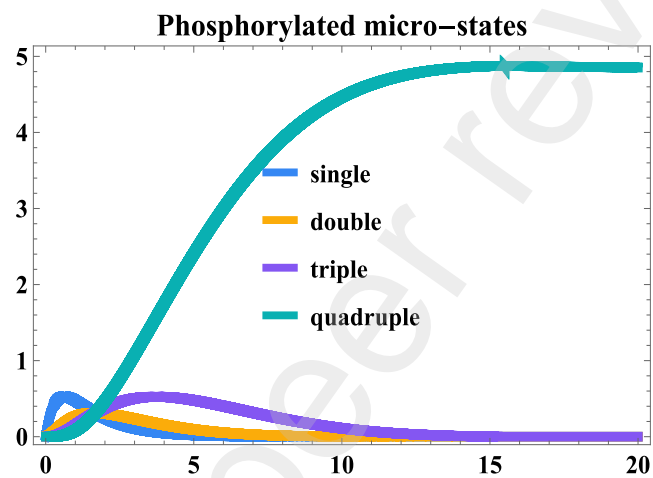


Figure 12. Phosphorylated micro-states for AnkG binding model.

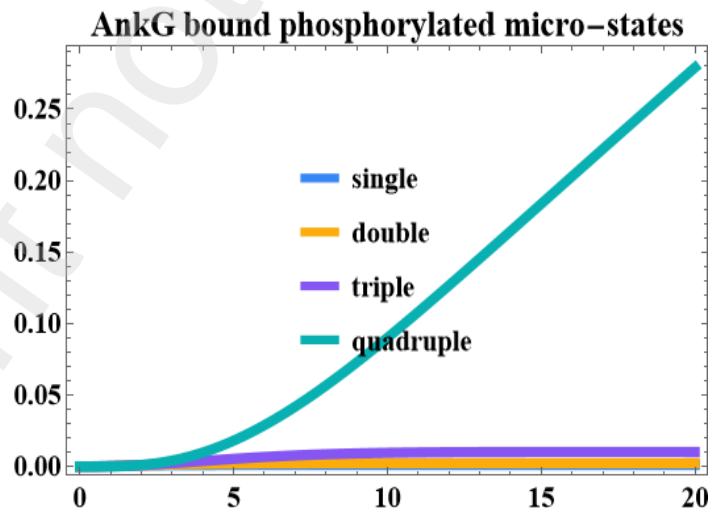


Figure 13. AnkG bound micro-states that are bound to the AIS.

While phosphorylated micro-states are quick to increase, slower increase of AnkG bound micro-states is expected for the given set of coefficients. If AnkG is mutated in a decaying exponential curve given in Figure 14, the corresponding AnkG bound micro-states cease to increase as shown in Figure

15. When AnkG approaches to zero the previously described CK2 phosphorylation model takes over the dynamics instead of AnkG binding model and we need to switch over to the phosphorylation model to compute the macro- and micro-states variables when AnkG=0 by taking appropriate initial conditions.

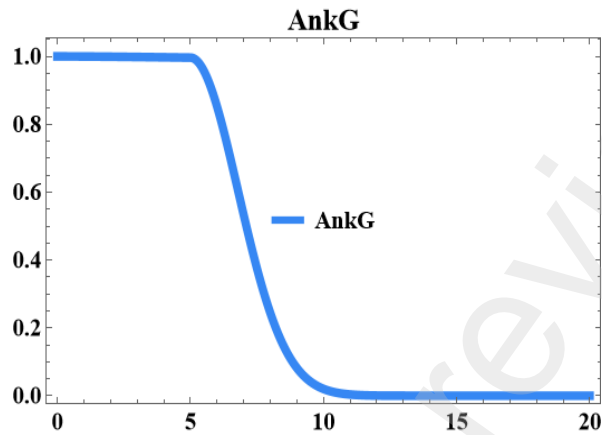


Figure 14. AnkG reduction imposed on the model to produce a response given in Figure 15.

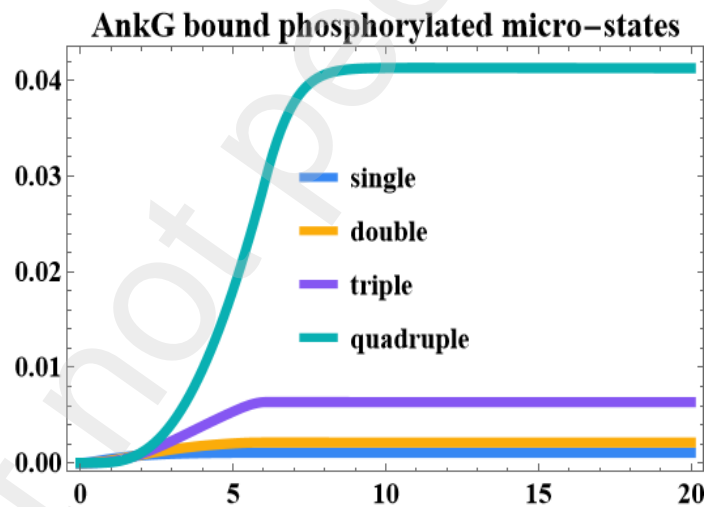


Figure 15. Response curves of AnkG bound micro-states to AnkG mutation shown in Figure 14.

The computational experiments done on the model—results are not shown for brevity--- show that binding and unbinding kinetic coefficients related AnkG play a major role in the levels of AnkG bound Nav, and the relationships of different levels of phosphorylation of Nav channels and AnkG binding are complex given the fluctuations present in and around AIS region. The model can be used to test different scenarios related to coefficients and initial conditions.

4. All time trajectories can be expressed with a single functional form

Since a large number of parameters are in the models developed, we explored many functions by trial and error to fit the time profiles of all the variables in the models so that we could simplify the parameter space to a few parameters. We use “NonlinearFit” function in Mathematica® extensively for this purpose and the following functional form fit all the trajectories with adjusted R^2 values >0.9 , and in many cases $R^2 >0.99$.

$$\text{Variable of interest} = f(t) = \frac{\gamma}{(\sqrt{2\pi}) \sigma t} e^{-\frac{(-\mu + \text{Log}_{10}(t))^2}{2\sigma^2}} \quad (45)$$

where t is time, γ , μ , and σ are parameters to be estimated using the data from simulations.

Eq. (45) has the form of log normal distribution, and it also depicts plateauing of curves very well. The graphs of these curves with the simulated data overlap almost perfectly in almost all cases. We do not understand the mathematical basis for this fit except to say that this may be purely a statistical feature. Utility value of Eq. (25) is that time trajectories can be compared across many regimes of kinetic coefficients using just three parameters. In the next section, we illustrate this without resorting to graphs.

5. Incorporation of in vitro experimental insights

We have not used actual experimental values for the parameters of the model as they are rare in the literature, and a theoretical model may be more useful in understanding the complexities involved. However, in this section, we use numerical values for the coefficients and initial conditions by adapting the in-vitro experimentally reported values in the literature. Caveat is that these reported values come from diverse sources related to multitude of neuronal types and experimental objectives. Stuart and Kole (2012) reported that the total number of Nav channel bound to AnkG on the AIS ranges from 100 to 300 per μm of AIS. (Length and diameter of AIS region are $<100 \mu\text{m}$ and $\sim 1.5 \mu\text{m}$, respectively.) We can safely assume that the initial number of Nav channels is around ~ 300 per μm and AIS volume is $\sim 100 (\mu\text{m})^3$ (Jones and Svitkina, 2016); this gives $0.05 \mu\text{M}$ of Nav as the initial value, and Srinivasan et al., (1988) estimated that AnkG numbers are 10 times higher than those of Nav channels, hence we assume $0.5 \mu\text{M}$ to be the initial value of AnkG. We do not have data on CK2 numbers, but it is always in abundance, and we assume initial concentration of CK2 of $1 \mu\text{M}$. Guided by the values given by Ubersax and Ferrell (2007), $k_{\text{fai}} \sim 1 \mu\text{M}^{-1} \text{s}^{-1}$ and $k_{\text{rai}} (\ll k_{\text{fai}}) \sim 10^{-6} - 10^{-3} \text{s}^{-1}$; AnkG kinetic binding coefficients in $\mu\text{M}^{-1} \text{s}^{-1}$: for s1110, s1101, and 1011 is 2×10^{-3} ; for s0111, is 1×10^{-3} ; for s1111, is 4×10^{-3} ; for {s1100, s1001, s1010}, is 1×10^{-4} . Guided by the values given by Brechet et al., (2008); AnkG unbinding coefficients are around $1 \times 10^{-6} \text{s}^{-6}$; and binding coefficients for other microstates are reported to be negligible. In our simulations we attempt to keep the relativities of AnkG related kinetic coefficients same as the experimentally reported values, but we experiment with diverse range of values.

The computational experiment with the coefficients that are representative of in-vitro data for AnkG binding was run and the parameters for Eq. (45) are estimated (Table 2) with the given model

coefficients and initial conditions. Then we increased the coefficients related to AnkG binding and ran the model and the parameters for Eq. (45) are estimated

Variable	γ	μ	σ	R^2
s1111A	0.220061	4.45612	0.90894	0.9999
s1110A	0.000698	2.97334	0.83945	0.9999
s0111A	0.000347	2.97334	0.83945	0.9999
s1100A	0.000014	3.08938	1.07632	0.9995
s1111	1.396280	2.98283	0.84210	0.9999
s1110	0.025839	1.33656	0.60598	0.9972
s1100	0.008676	0.69048	0.66712	0.9929
s1001	0.008676	0.69048	0.66712	0.9929

Table 2. The estimated parameters for Eq. (45) for the following coefficients and initial conditions:

Nav initial concentration=0.05; CK2(0)=1.0; kfa1=1.0;kra1=0.001; kfa2=1.00; kra2=0.001;kfa3=1.0;kra3=0.001;kfa4=1.0; kra4=0.001; AnkG(0)=0.5; kfl110=0.002; kr1110=1.0*10⁻⁶; kfl101=0.002; kr1101=1.0*10⁻⁶; kfl011=0.002; kr1011=1.0*10⁻⁶; kfl1010=0.0001; kr1010=1.0*10⁻⁶; kfl100=0.0001; kr1100=1.0*10⁻⁶; kfl010=0.0001; kr1010=1.0*10⁻⁶; kfl0111=0.001; kr0111=1.0*10⁻⁶; kfl1111=0.004;kr1111=1.0*10⁻⁶; kfl0000=0.000001;kfl0100=0.00001;kfl0010=0.00001;kfl0110=0.001;kfl0001=0.00001;kfl0101=kfl0011=0.001;kfl1000=0.00001;kfl1001=0.001; kr0000=0.000001;kr1001=0.0001;kr0100=kr0010=kr0110=kr0001=kr0101=kr0011=kr1000=0.000001.;

Variable	γ	μ	σ	R^2
s1111A	3.25495	3.5139	0.7518	0.9999
s1110A	0.03006	2.5436	0.7674	0.9991
s0111A	0.01503	2.5436	0.7674	0.9991
s1100A	0.00113	2.9691	1.0763	0.9989
s1111	0.47075	2.2954	0.6546	0.9993
s1110	0.01653	1.0811	0.4708	0.9700
s1100	0.00776	0.6129	0.6244	0.9857
s1001	0.00776	0.6129	0.6244	0.9857

Table 3. The estimated parameters for Eq. (45) for the following coefficients and initial conditions:

Nav(0)=0.05;CK2(0)=1.0; kfa1=1.0;kra1=0.001;kfa2=1.00;kra2=0.001;kfa3=1.0;kra3=0.001;kfa4=1.0;kra4=0.001;AnkG(0)=0.5;
kfl110=0.2;kr1110=1.0*10⁻⁴;kfl101=0.2;kr1101=1.0*10⁻⁴;kfl011=0.2;kr1011=1.*10⁻⁴;kfl010=0.01;kr1010=1.0*10⁻⁴;kfl100=0.01;
kr1100=0.0001;kfl010=0.01;kr1010=1.0*10⁻⁴;kfo111=0.1;kr0111=1.0*10⁻⁴; kfl111=0.4;
kr1111=0.0001;kfo000=0.001;kfo100=0.001;kfo010=0.001;kfo110=0.001;kfo001=0.001;kfo101=kfo011=0.1;kf1000=0.001;kf1001=0.1;kr0000=0.0000
1;kr1001=0.0001;kr0100=kr0010=kr0110=kr0001=kr0101=kr0011=kr1000=0.0001;

We see that the kinetic data that generated Table 2 give rise to lesser AnkG binding to s1111 than for those of the kinetic coefficients related to Table 3. In both cases, s1110A and s01111A have the same μ and σ values but γ values differ showing the effects of a1 phosphorylation on AnkG binding. At the same time, s1100 and s1001 have the same values for the three parameters as expected of CK2 phosphorylation. We can perhaps discuss kinetics of complex processes modelled in this paper in terms of Eq. (45) instead of deriving kinetic coefficients experimentally. This needs to be verified through experiments though.

6. Summary and conclusion

We develop a theoretical model for CK2 phosphorylation of Nav channels using a conceptual model of Nav channels and extend the model for AnkG binding to the phosphorylated sites in Nav within AIS. This theoretical model based on mass action kinetics of micro- and macro- states shows the crucial role AnkG play as a master organiser by getting Nav bound to AIS membrane. Hence AnkG as a key player in AD pathology for example can be easily understood from this theoretical study. This study perhaps guides the experimentalist to understand the roles of AIS in generating action potential, and in future, we could develop a mechanistic approach to understand the action potential generation using a biochemical basis to better understand the electrical analogies that currently in use.

Acknowledgements

The author is grateful to Dr. A. Pashang for the help in preparing Figures 1-4.

References

- Bi C, Wu J, Jiang T, Liu Q, Cai W, Yu P, Cai T, Zhao M, Jiang Y H, Sun ZS (2012) Mutations of ANK3 identified by exome sequencing are associated with autism susceptibility. *Hum Mutat* 33:1635-1638.
- Bian Y, Ye M, Wang C, Cheng K, Song C, Dong M, Pan Y, Qin H, Zou H (2013). Global screening of CK2 kinase substrates by an integrated phosphoproteomics workflow. *Sci Rep* 3:1-7.
- Borisov, Nikolay M., Nick I. Markevich, Jan B. Hoek, and Boris N. Kholodenko (2005) Signaling through Receptors and Scaffolds: Independent Interactions Reduce Combinatorial Complexity *Biophysical Journal* Volume 89:951–966.
- Bréchet A, Fache MP, Brachet A, Ferracci G, Baude A, Irondelle M, Pereira S, Leterrier C, Dargent B (2008) Protein kinase CK2 contributes to the organization of sodium channels in axonal membranes by regulating their interactions with ankyrin G. *J. Cell Biol* 183:1101-1114.
- Buffington SA, Rasband MN (2011) The axon initial segment in nervous system disease and injury. *Eur J Neurosci* 34:1609-1619.
- Catterall, W. A. (2014). Structure and function of voltage-gated sodium channels at atomic resolution. *Exp Physiol* 99.1. pp 35–51
- Cantrell AR, Scheuer T, Catterall WA (2018) Voltage-dependent neuromodulation of Na⁺ channels by D1-like dopamine receptors in rat hippocampal neurons. *J Neurosci* 19:5301-5310.
- Cunha SR, Mohler PJ (2009) Ankyrin protein networks in membrane formation and stabilization. *J Cell Mol Med* 13(11-12):4364-4376.
- Diana Sa´nchez-Ponce, Lidia Bla´zquez-Llorca, Javier DeFelipe, Juan Jose´ Garrido and Alberto Muñoz. (2012) Colocalization of a-actinin and Synaptopodin in the Pyramidal Cell Axon Initial Segment. *Cerebral Cortex* July 2012;22:1648-1661.doi:10.1093/cercor/bhr251

- Fache MP, Moussif A, Fernandes F, Giraud P, Garrido J, Dargent B (2004) Endocytotic elimination and domain-selective tethering constitute a potential mechanism of protein segregation at the axonal initial segment. *J Cell Biol* 166:571-578.
- Fan X, Markram H (2019) A brief history of simulation neuroscience. *Front Neuroinform* 13:32.
- Gulledge AT, Bravo JJ (2016) Neuron Morphology Influences Axon Initial Segment Plasticity. *eNeuro* 3. pii: ENEURO.0085-15.2016.
- Harty RC, Kim TH, Thomas EA, Cardamone L, Jones NC, Petrou S, Wimmer VC (2013) Axon initial segment structural plasticity in animal models of genetic and acquired epilepsy. *Epilepsy Res* 105:272-279.
- Hedstrom KL, Ogawa Y, Rasband MN (2008) AnkyrinG is required for maintenance of the axon initial segment and neuronal polarity. *J Cell Biol* 183:635-640.
- Jones SL, Svitkina TM (2016) Axon initial segment cytoskeleton: architecture, development, and role in neuron polarity. *Neural Plast* 2016:6808293.
- Kaphzan H, Buffington SA, Jung JI, Rasband MN, Klann E (2011) Alterations in intrinsic membrane properties and the axon initial segment in a mouse model of angelman syndrome. *J Neurosci* 31:17637-17648.
- Kole MH, Ilschner SU, Kampa BM, Williams SR, Ruben PC, Stuart GJ (2008) Action potential generation requires a high sodium channel density in the axon initial segment. *Nat Neurosci* 11:178-186.
- Kole MH, Stuart GJ (2012) Signal processing in the axon initial segment. *Neuron* 73:235-247.
- Kim DY, Carey BW, Wang H, Ingano LA, Binshtok AM, Wertz MH, Pettingell WH, He P, Lee VM, Woolf CJ, Kovacs DM (2007) BACE1 regulates voltage-gated sodium channels and neuronal activity. *Nat Cell Biol* 9:755-764.
- Kovacs DM, Gersbacher MT, Kim D (2010) Alzheimer's secretases regulate voltage-gated sodium channels. *Neurosci Lett* 486:68-72.
- Lemaitre G, Barbara W, Stephen L (2003). Identification of a Conserved Ankyrin-Binding Motif in the Family of Sodium Channel α Subunits. *Journal of Biological Chemistry* 278(30): 27333-39.
- Leterrier C, Dargent B (2014) No Pasaran! Role of the axon initial segment in the regulation of protein transport and the maintenance of axonal identity. *Semin Cell Dev Biol* 27:44-51.
- Leterrier C, Potier J, Caillol G, Debarnot C, Rueda Boroni F, Dargent B (2015) Nanoscale architecture of the axon initial segment reveals an organized and robust scaffold. *Cell Rep* 13:2781-2793.
- Mathematica® (2025) Version 14.2. Wolfram.com
- Meggio F, Pinna LA (2003) One-thousand-and-one substrates of protein kinase CK2. *J FASEB* 17:349-368.
- Nakata T, Hirokawa N (2003) Microtubules provide directional cues for polarized axonal transport

- through interaction with kinesin motor head. *J Cell Biol* 162:1045-1055.
- Nelson AD, Jenkins PM (2017) Axonal membranes and their domains: assembly and function of the axon initial segment and node of Ranvier. *Front Cell Neurosci* 11:1-17.
- Nishi H, Shaytan A, Panchenko AR (2014) Physicochemical mechanisms of protein regulation by phosphorylation. *Front Genet* 5:1-10.
- Peltola MA, Kuja-Panula J, Liuhanen J, Vöikar V, Piepponen P, Hiekkalinna T, Taira T, Lauri SE, Suvisaari J, Kuleskaya N, Paunio T, Rauvala H (2016) AMIGO-Kv2.1 potassium channel complex is associated with schizophrenia-related phenotypes. *Schizophr Bull* 42:191-201.
- Rasband MN (2008) Na⁺ channels get anchored...with a little help. *J Cell Biol* 183:975-977.
- Rasband MN (2009) Converging on the origins of axonal ion channel clustering. *PLoS Genet* 5:e1000340.
- Salazar C. and Hofer T. (2009) Multisite protein phosphorylation – from molecular mechanisms to kinetic models. *The FEBS Journal* 276: 3177–3198.
- Sa'nchez -Ponce D, Muñoz A, Garrido JJ (2011) Casein kinase 2 and microtubules control axon initial segment formation. *Mol Cell Neurosci* 46:222-234.
- Schafer DP, Jha S, Liu F, Akella T, McCullough LD, Rasband MN (2009) Disruption of the axon initial segment cytoskeleton is a new mechanism for neuronal injury. *J Neurosci* 29:13242-13254.
- Stepanov A., Tatiana Karelina, Nikolai Markevich, Oleg Demin, Timothy Nicholas (2018) A mathematical model of multisite phosphorylation of tau protein. *PLoS ONE* 13(2): e0192519. <https://doi.org/10.1371/journal.pone.0192519>
- Srinivasan Y, Elmer L, Davis J, Bennett V, Angelides K (1988) Ankyrin and spectrin associate with voltage-dependent sodium channels in brain. *Nature* 333:177-180
- Sun X, Wu Y, Gu M, Zhang Y (2014) MiR-342-5p decreases ankyrin G levels in Alzheimer's disease transgenic mouse models. *Cell Rep* 6:264-270.
- Ubersax JA, Ferrell JE (2007) Mechanisms of specificity in protein phosphorylation. *Nat Rev Mol Cell Biol* 8:530-541.
- Xu M, Cooper E C (2015) An Ankyrin-G N-terminal Gate and Protein Kinase CK2 Dually Regulate Binding of Voltage-gated Sodium and KCNQ2/3 Potassium Channels. *J Biol Chem* 290:16619-16632.
- Zhang X, Bennett V (1998) Restriction of 480/270-kD ankyrin G to axon proximal segments requires multiple ankyrin G-specific domains. *J Cell Biol* 142:1571-1581.
- Zhou D, Lambert S, Malen PL, Carpenter S, Boland LM, Bennett V (1998) Ankyrin(G) is required for clustering of voltage-gated Na channels at axon initial segments and for normal action potential firing. *J Cell Biol* 143:1295-1304.